

Geological, tomographic, kinematic and geodynamic constraints on the dynamics of sinking slabs

N.P. Butterworth^{a,*}, A.S. Talsma^a, R.D. Müller^a, M. Seton^a, H.-P. Bunge^b, B.S.A. Schuberth^b, G.E. Shephard^a, C. Heine^a

^a EarthByte Group, School of Geosciences, The University of Sydney, New South Wales 2006, Australia

^b Department of Earth and Environmental Science, Ludwig-Maximilians-Universität München, Germany



ARTICLE INFO

Article history:

Received 24 July 2012

Received in revised form 22 October 2013

Accepted 23 October 2013

Available online 1 November 2013

Keywords:

Subduction

Geodynamic modeling

Mantle convection

Tomography

Sinking rate

ABSTRACT

We use geodynamic models with imposed plate velocities to test the forward-modeled history of subduction based on a particular plate motion model against alternative seismic tomography models. We utilize three alternative published reference frames: a hybrid moving hotspot-palaeomagnetic, a hybrid moving hotspot-true polar wander corrected-palaeomagnetic, and a Subduction Reference Frame, a plate model including longitudinal shifts of subduction zones by matching subduction volumes imaged by P-wave tomography, to assess which model best predicts present day mantle structure compared with seismic tomography and volumetrically derived subduction history. Geodynamic modeling suggests paleo-longitudinal corrections applied to the Subduction Reference Frame result in lower mantle slab material beneath North America and East Asia accumulating up to 10–15° westward of that imaged by tomography, whereas the hybrid models develop material offset by 2–9°. However, the Subduction Reference Frame geodynamic model produces slab material beneath the Tethyan Domain coinciding with slab volumes imaged by tomography, whereas the hybrid reference frame models do not, suggesting regional paleo-longitudinal corrections are required to constrain slab locations. We use our models to test inferred slab sinking rates in the mantle focusing on well-constrained regions. We derive a globally averaged slab-sinking rate of 13 ± 3 mm/yr by combining the ages of onset and cessation of subduction from geological data and kinematic reconstructions with images of subducted slabs in the mantle. Our global average slab-sinking rate overlaps with the 15–20 mm/yr rate implied by mantle convection models using a lower mantle viscosity 100 times higher than the upper mantle.

© 2013 Elsevier Ltd. All rights reserved.

1. Introduction

Plate tectonic absolute reference frames are essential for linking plate motions and the history of subduction to mantle dynamics—yet they are subject to substantial ambiguities, reflecting uncertainties in paleomagnetic and hotspot track data. Additional constraints on absolute plate motion can be derived by considering the inherent connection between plate boundaries and the history of subduction reflected by tomographically interpreted subducted slabs in the mantle. Over the last decade, our knowledge about relative motion between the major tectonic plates has increased substantially, primarily due to advances in seafloor mapping and data coverage. Absolute plate motions, which anchor relative plate motions to a fixed reference frame in the Earth's interior, are still controversial as different approaches advocate alternative absolute plate positions through time. Previous

attempts to construct absolute reference frames have fallen into two primary camps: those based on palaeomagnetic data (e.g. Torsvik et al., 2008b) and those based on hotspots (e.g. O'Neill et al., 2005). Paleomagnetic data can be used to determine the paleo-meridian orientation and paleolatitude of a plate, which together can be used to derive total reconstruction poles. However, since the Earth's magnetic dipole field is radially symmetric, no paleo-longitudinal information can be deduced from paleomagnetic data (Torsvik et al., 2008a). Seamount chains with a linear age progression (i.e. hotspot tracks) can be used to restore plates to their paleo-positions with the assumption that hotspots are either fixed or nearly fixed relative to each other ("fixed hotspot hypothesis") (Morgan, 1983). Continuous hotspot chains that extend beyond 100 Ma are rare, and there is observational and geodynamic modeling evidence suggesting hotspots have moved relative to each other (Steinberger and O'Connell, 1997; Tarduno et al., 2003; O'Neill et al., 2005). Numerous paleomagnetic datasets and models for the "absolute" motions of the North American, African and Eurasian plates during the Mesozoic and Cenozoic have been published and they reveal various inconsistencies between different apparent polar

* Corresponding author. Tel.: +61 293518093.

E-mail address: nathaniel.butterworth@sydney.edu.au (N.P. Butterworth).

wander (APW) paths, some corrected for true polar wander, and hotspot models, especially for times older than about 100–80 Ma (Steinberger and Torsvik, 2008; Torsvik et al., 2008b).

Discriminating between alternative approaches is difficult without a series of tie-points between the surface and the underlying mantle. The idea that the inferred location of subduction zones through time could be reconciled with tomographically imaged locations of subducted slab material in the Earth's lower mantle ("slab graveyards" Richards and Engebretson, 1992) led to a new generation of absolute plate motion model called Subduction Reference Frames (Van der Meer et al., 2010). Seismic tomography models allow visualization of subducted slabs, and can be used to validate geodynamic models of mantle convection. In order to utilize the history of subduction in the mantle as a constraint on absolute plate motions it is required to understand the regionally dependent sinking histories of so-called 'anchor' slabs. Information from the geological record that indicates beginning and cessation of subduction, as well as from geodynamic modeling, can be used together to unravel the history and dynamics of sinking lithospheric slabs and to construct and test the accuracy of Subduction Reference Frames (Sigloch and Mihalynuk, 2013).

We test three published hybrid models of absolute plate motion while keeping the relative plate motion model and geodynamic model parameters constant. This is done by imposing alternative absolute reference frame models as surface boundary conditions for a series of finite element forward geodynamic models. The models of plate motion tested included a hybrid moving hotspot-paleomagnetic reference frame (O'Neill et al., 2005; Torsvik et al., 2008a), a hybrid moving hotspot-paleomagnetic reference frame corrected for true polar wander (TPW) (O'Neill et al., 2005; Steinberger and Torsvik, 2008), and a Subduction Reference Frame (Van der Meer et al., 2010). Key subduction zones are examined to quantify regional latitudinal/longitudinal differences between absolute rotation models. Geodynamic model output is compared to four recent seismic tomography models for validation of stable features. Identification of tomographically imaged "reference" slabs, which are visible in many tomographic models regardless of inversion technique, as well as the slabs' relationship to surface kinematics is tantamount to further developing robust surface-deep mantle reference points. We examine age-depth relationships of subducted material and slab sinking rates within the mantle in order to use the record of subduction provided by seismic tomography as a constraint for absolute plate motion.

2. Methods

2.1. Plate kinematic models

To assess the implications of alternative reference frames, we use a coupled plate kinematic-mantle convection modeling approach, whereby the predicted present-day mantle structure is compared to seismic tomography models. We use a plate motion model as input into the geodynamic mantle convection code.

A plate motion model comprises relative motions between plates linked via a plate circuit to an absolute reference frame. The hierarchical nature of our plate model links the global plate circuit through Africa to the absolute reference frame. For the purposes of constructing the three alternate absolute reference frames, the relative plate rotation model from Müller et al. (2008) is used. This rotation hierarchy contains Euler poles describing motions of all major tectonic elements. One complication in using absolute plate motion models before 83.5 Ma is that the Pacific plate cannot be linked to the plate circuit via relative plate motions before this time, as the Pacific Ocean was entirely surrounded by subduction zones. Therefore the Pacific plate is reconstructed between 83.5 and 140 Ma based on the absolute plate rotation model by Wessel et al. (2006), which is based on fixed Pacific hotspots, and moves independently to the hotspots in the Indian-Atlantic realm. A recent paper by Doubrovine et al. (2012) attempted to create a global reference model to overcome this limitation and this will be tested as part of a further study.

We use realistic, evolving plate boundaries and motions, termed "dynamically closing" or "continuously closing" plate polygons through time (Gurnis et al., 2012) and utilize a set of plate topologies, which consist of paleo and current mid ocean ridges, subduction zones and transform plate boundaries, constructed using the GPlates software package (www.gplates.org). The same set of topological plate boundaries is used for all three alternate models, and as such, only the relative position of the plates differs between models (Fig. 1).

2.1.1. Hybrid moving hotspot and paleomagnetic reference frame model

This model utilizes the moving Indo-Atlantic hotspots of O'Neill et al. (2005) to constrain absolute plate motion between 100–0 Ma, while paleomagnetic constraints of Torsvik et al. (2008a) were used between 140 and 100 Ma. For the purpose of this model, Africa

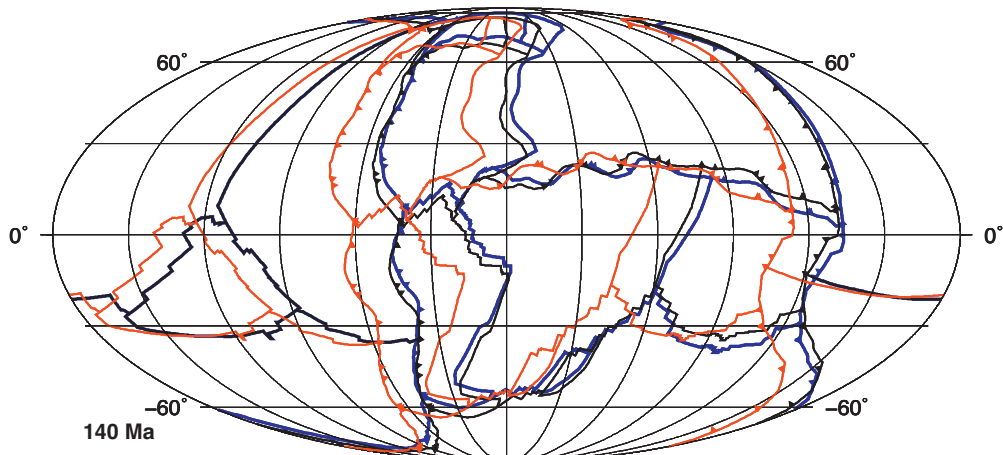


Fig. 1. Longitudinal differences between the three alternate models of absolute plate motion at 140 Ma, showing the initial plate configuration for each Terra model input, with red lines corresponding to reconstructed plate boundaries using the subduction Reference Frame, black lines are the Hybrid TPW Paleomagnetic reference frame, and blue lines are the Hybrid Paleomagnetic reference frame. TPW is only applied to the African hemisphere as there is no link to the Pacific prior to 83.5 Ma, hence the two paleomagnetic reference frames are identical inside the Pacific basin. Triangles on the lines represent subduction zones. (For interpretation of the references to color in this figure legend, the reader is referred to the web version of the article.)

is held as longitudinally fixed between 140 and 100 Ma, which is based on the assumption that Africa has been surrounded by mid ocean ridges during this time. Geodynamic output based on this reference frame will referred to as the Hybrid Paleomagnetic model.

2.1.2. Hybrid moving hotspot and TPW corrected paleomagnetic reference frame model

The moving Indo-Atlantic hotspot model of O'Neill et al. (2005) was used in order to constrain the absolute rotations of Africa from the period of 100–0 Ma. For times between 140 and 100 Ma, a true polar wander corrected paleomagnetic reference frame was used derived from Steinberger and Torsvik (2008). As the motion of the poles is known to be quite stable for the past 100 Myr, due to a general decrease in the amount of subduction at polar latitudes and increase at equatorial latitudes (Steinberger and Torsvik, 2010), corrections are not applied from 100 Ma to the present. Even so, use of the hotspot reference frame after 100 Ma negates the requirement for true polar wander correction in this time period. The geodynamic model resulting from this reference frame will henceforth be called the Hybrid TPW Paleomagnetic model.

2.1.3. Subduction Reference Frame model

The rotations of Van der Meer et al. (2010) were used in order to construct a Subduction Reference Frame model. The Subduction Reference Frame is based on the same TPW corrected paleomagnetic absolute reference frame used in this study (O'Neill et al., 2005; Steinberger and Torsvik, 2008) but with additional absolute longitudinal corrections to the absolute position of Africa between 140 Ma and present day. The model utilizes tomographic model UU-P07 (Amaru, 2007), a global P-wave tomography model, to isolate positive velocity anomalies in the lower mantle interpreted as subducted slabs. It longitudinally corrects Africa's absolute rotations by correlating deep mantle tomographic anomalies with surficial geological evidence of past subduction events, assuming that material sinks vertically in both the upper and lower mantle. It uses three primary anchor slabs in order to correct for this longitudinal mismatch: the Aegean Tethys, the Mongol-Okhotsk and the Farallon slab, to correct rotations from the Permo-Triassic to the present day. Their analysis found longitudes to be most offset from the TPW paleomagnetic reference frame during the mid Mesozoic, requiring corrections of up 18° during this time. We note that the applied longitudinal shift removes the fit to the hotspot record. The geodynamic model resulting from this reference frame will be referred to as the Subduction Reference Frame model.

2.2. Global mantle convection models

In order to simulate mantle convection through time, we use the parallel 3D finite element code, Terra (Bunge and Baumgardner, 1995; Bunge et al., 1996, 1997; Oeser et al., 2006). Terra solves the equations that govern the conservation of mass, momentum and energy for a highly viscous fluid (appropriate for the mantle) at infinite Prandtl number in a 3D spherical shell in a compressible form. The modeling domain is discretized with a mesh derived from the icosahedron to assure an almost uniform grid spacing at each radial level with a grid resolution of 30 km at the surface and ~25 km in the radial direction. The high numerical resolution allows us to model mantle flow at Earth-like convective vigor, expressed by a thermal Rayleigh number of ~10⁹ based on internal heating. Input parameters, given in Table 1, are equivalent to Schuberth et al. (2009a).

We divide the Earth's mantle into three layers; the lithosphere, and the upper and lower mantle, in order to represent its radially varying material properties. The assigned viscosities are 10²³, 10²¹ and 10²³ Pa s, respectively. The layers are separated at 100 km and 660 km, numbers inferred as first order rheological stratification

Table 1
Variables kept constant between model runs.

Variable	Value	Units
Outer shell radius	6370	km
Inner shell radius	3480	km
Surface temperature	300	K
Basal temperature	4200	K
Internal heating rate	6.0 × 10 ⁻¹²	W kg ⁻¹
Heat capacity	1.134 × 10 ³	J kg ⁻¹ K ⁻¹
Thermal expansivity (surface)	4.011 × 10 ⁻⁵	K ⁻¹
Thermal expansivity (CMB)	1.256 × 10 ⁻⁵	K ⁻¹
Thermal Conductivity	3.0	W m ⁻¹ K ⁻¹
Reference Viscosity	1.0 × 10 ²¹	Pa s
Rayleigh number	~10 ⁹	

boundaries in the mantle based on geoid studies and post-glacial rebound (Hager and Richards, 1989; Paulson et al., 2007). We use only radial viscosity layering, with no lateral variation. Including temperature dependant viscosity was beyond the scope of this study, but would serve to localize the coherency of slabs, increasing upper mantle sinking speed by a few 10's of percent. In the lower mantle however, it would have negligible effect on slab sinking rates, but might affect slab morphology leading to less internal deformation and thus more accurate comparisons with tomography.

Temperature is kept constant at the surface (300 K) and the CMB (4200 K), with the CMB temperature chosen to yield global mantle flow with strong plume flux (Bunge, 2005). A dynamic regime dominated by thermal structure provides a good match to seismic tomography in terms of heterogeneity strength (Schuberth et al., 2009a,b) and radial profiles (Styles et al., 2011). Mechanical boundary conditions are free slip at the CMB. At the surface, velocities are imposed using pre-generated plate kinematic models. Velocities are specified at the surface and assimilated using a sequential data assimilation method (Talagrand, 1997). This is done in order to allow material to be input into the mantle at reasonable rates known from present day plate velocities (Schuberth et al., 2009b). Subduction zones therefore evolve at areas of convergence through time, where linear downwellings are pulling on the overriding cold material. Sinking is dynamically computed following from solving the conservation equations. As the structure of the mantle in the geological past is essentially unknown, the choice of initial mantle condition is necessarily arbitrary. Here, the unknown conditions of mantle heterogeneity at the model start time are approximated by running convection with global plate configurations fixed to the 140 Ma reconstruction of each absolute plate motion model until a quasi steady thermal state is reached (Bunge et al., 2002). The relative location for each model's plate boundaries and subduction zones at 140 Ma is shown in Fig. 1.

Endothermic phase transitions at 660 km are not included in this study, as the appropriate parameters (i.e. Clapeyron slopes) to use are not obvious due to the effects of different mineralogies, complex multiphase components and the presence of water. Phase transitions would likely have the net affect of increasing mantle residence time of sinking slabs, including them was beyond the scope of this study.

2.3. Tomography models

Seismic tomography provides a means of imaging the deep earth based on heterogeneities in seismic wave speed received at the Earth's surface. As numerous inversion methods exist for constructing tomographic models we compare our model output to multiple tomography models based on different approaches and data to emphasize common stable features between models and avoid over interpretation of any one model. We utilize two P-wave models,

MIT-P08 (Li et al., 2008) and Montelli-P (Montelli et al., 2004), and two S-wave models, GyPSuM-S (Simmons et al., 2010) and s40rts (Ritsema et al., 2010).

2.3.1. MIT-P08

The MIT-P08 seismic tomography model of Li et al. (2008) utilizes P-wave travel time residuals computed from ak135 (Kennett et al., 1995). As it is based on P-wave data, MIT-P08 displays the best resolution near seismic receiver-rich areas (i.e. well instrumented subduction zones). It is appropriate for imaging upper mantle structures such as subducting lithospheric slabs, but lacks resolution in receiver-poor ocean basins and in the deeper mantle (Li et al., 2008).

2.3.2. Montelli-P

The Montelli-P tomographic model utilizes finite-frequency sensitivity kernels to account for the effects of wavefront healing on low frequency P-waves in order to better resolve small-scale (i.e. slab and plume, sub-Fresnel zone, sized) structures in the deep mantle (Montelli et al., 2004). Being a P-wave model, data coverage is best near subduction zones and receiver rich areas; however it includes both long and short period P-wave data sets.

2.3.3. GyPSuM-S

The GyPSuM-S model utilizes data from a wide range of geo-physical sources. It simultaneously inverts S and P wave seismic data as well as geodynamic constraints (i.e. constraints from free-air gravity, plate motions, dynamic topography and core ellipticity) in order to better account for non-thermal heterogeneity (Simmons et al., 2010).

2.3.4. s40rts

s40rts is an S-wave based tomographic model that focuses on maximizing data coverage in the mantle, especially over receiver poor areas, utilizing 3D perturbations of isotropic shear velocity with respect to the Preliminary Reference Earth Model (Ritsema et al., 2010). s40rts differs from previous approaches in that it uses a data set larger by an order of magnitude compared to s20rts, hence offering higher spatial resolution than previous models. This leads to an improved resolution in areas away from subduction zones (i.e. in the oceans, stable areas distal from active plate margins, receiver poor areas).

3. Results

Our aims are two fold—to examine the implications of different absolute reference frame models in a global geodynamic model, and to use geodynamic model results to constrain the relationship between tomographically imaged slabs and surface plate kinematics. In order to examine how well different absolute reference frames reproduce observations made from alternative tomographic images of the mantle, three modeled scenarios of absolute plate motion and the four alternate tomography models are compared and analyzed. The relationship between kinematics and tomographically identified slabs inherently provides information about slab sinking (Steinberger et al., 2012), thus providing an important constraint for absolute plate motion by demonstrating visible tie points between the subducting lithosphere at Earth's surface and the deep mantle. Furthermore, inferences about slab sinking rates and mantle viscosity can be made, allowing a more accurate comparison between geodynamic models and tomography models.

We follow the approach of Van der Meer et al. (2010) and correlate areas where the onset and cessation of subduction are relatively well constrained by geological data, such as ophiolite obduction and arc magmatism, to seismic anomalies interpreted as

Table 2

Reinterpreted age assignments for the base and top of subducted slabs interpreted in Van der Meer et al. (2010). Depths are those listed in Van der Meer et al. (2010) derived from tomography model UU-P07 (Amaru, 2007).

Model	UU-P07					
	Age (Ma)		Base (km)		Top (km)	
	Slab name	Base	Top	Min	Max	Min
Aegean Tethys	170	0	2100	1900	0	0
Aleutian	50	0	810	710	0	0
Beaufort	200	155	2650	2480	2300	2100
Chukchi	160	130	1900	1700	1325	1175
East China	200	158	2900	2815	1900	1700
Farallon	185	60	2650	2480	920	710
Himalayas	80	30	1175	1040	500	440
Kamchatka	60	0	920	810	0	0
Maldives	180	80	2300	2100	920	810
Manchuria	50	0	920	810	0	0
Mesopotamia	165	80	2300	2100	1175	1040
Mongol Okhotsk	—	150	2900	2815	1900	1700
Mongolia	165	80	1900	1700	1175	1040
Sakhalin	65	50	1175	1040	810	710

subducted slabs common in multiple tomography models. Depths are derived from four alternate tomography models, two P-wave models MIT-P08 (Li et al., 2008) and Montelli-P (Simmons et al., 2010) and two S-wave models GyPSuM-S (Simmons et al., 2010) and s40rts (Grand, 1994), plus we include the interpretations of Van der Meer et al. (2010) determined with UU-P07 (Amaru, 2007). Derived slab depths can be seen in Tables 2–4. ‘Slabs’ are picked from where there is a sharp change in the positive seismic anomalies evident in the tomography models (Supplementary Information). We define this as being one standard deviation away from the median seismic velocity anomaly in each tomography model. We determine these contour values to be +0.6% for s40rts, +0.2% for MIT-P08, +0.6% for GyPSuM-S, and +0.3% for Montelli-P. Slabs in the Terra models are determined in a similar fashion, resulting in a -200 K temperature anomaly contour. Ages are reinterpreted where the base plate kinematic model (Müller et al., 2008) differed substantially from the interpretation of Van der Meer et al. (2010) (Table 2). While Van der Meer et al. (2010) included a total of 28 slabs, only those which are relatively well constrained in our models are reinterpreted. An effort was made to avoid slabs that lay along the CMB, as lateral spreading here would serve to artificially decrease a whole mantle sinking rate average. Even with the choice of well-constrained slabs and a quantitative approach to define a slab, the depth and location variation between models is apparent. We state the depth uncertainty (Tables 2–4) between an assumed max and minimum value based on each tomography model’s published depth slices, however the uncertainty is likely to be poorer than the errors we have stated. This is due to a number of reasons; firstly, determining model resolution is not straightforward (Lévéque et al., 1993). Slab dip and slab thickening will also influence the apparent slab depth (Van der Meer et al., 2010). Finally, matching the correct latitudinal subducted slab point with the surface timing point is impossible without a thorough understanding of the slab’s evolution. To minimize these issues, we use a process of determining slab depths in an iterative manner to qualitatively correlate the surface geological constraints and the corresponding point on the subducted slab. This was achieved by analysing the location of geological constraints, plate boundary surface kinematics, subduction volume history, tomographically imaged slab locations, and geodynamic model slab location results (Supplementary Information).

We initially discuss the subduction history of each region and relate it to tomography, and then discuss the geodynamic modeling results.

Table 3

Reinterpreted depths of slabs from S-wave tomography models s40rts and GyPSuM-S. Min and Max values are inferred from an iterative interpretation (Supplementary Information) and are precise to the model's published depth slices.

Model	GyPSuM-S				s40rts			
	Base (km)		Top (km)		Base (km)		Top (km)	
Slab name	Min	Max	Min	Max	Min	Max	Min	Max
Aegean Tethys	2050	1900	0	0	2020	2000	0	0
Aleutian	850	750	0	0	440	420	0	0
Beaufort	2200	2050	1300	1150	2280	2260	1340	1320
Chukchi	2050	1900	1000	850	1680	1660	1260	1240
East China	2900	2650	1900	1750	2800	2800	1640	1620
Farallon	2500	2350	750	650	2200	2180	380	360
Himalayas	1150	1000	750	650	1000	980	480	460
Kamchatka	–	–	–	–	660	640	0	0
Maldives	2350	2200	1150	1000	2080	2060	1000	980
Manchuria	750	650	0	0	780	760	0	0
Mesopotamia	2200	2050	1300	1150	1980	1960	1020	1000
Mongol Okhotsk	2900	2650	2500	2350	2800	2800	2020	2000
Mongolia	1750	1600	1300	1150	2260	2240	1520	1500
Sakhalin	400	325	325	250	1000	980	440	420

Table 4

Reinterpreted depths of slabs from P-wave tomography models MIT-P08 and Montelli-P. Min and Max values are inferred from an iterative interpretation (Supplementary Information) and are precise to the model's published depth slices.

Model	MIT-P08				Montelli-P			
	Base (km)		Top (km)		Base (km)		Top (km)	
Slab name	Min	Max	Min	Max	Min	Max	Min	Max
Aegean Tethys	1649	1604	0	0	2020	2000	0	0
Aleutian	836	791	0	0	780	760	0	0
Beaufort	–	–	–	–	2160	2140	1380	1360
Chukchi	1830	1785	1468	1423	1920	1900	1080	1060
EastChina	2869	2869	1830	1785	2900	2900	1640	1620
Farallon	1830	1785	384	339	1800	1780	520	500
Himalayas	926	881	384	339	1080	1060	500	480
Kamchatka	1017	971	0	0	1500	1480	0	0
Maldives	2191	2146	926	881	2200	2180	840	820
Manchuria	746	700	0	0	880	860	0	0
Mesopotamia	2011	1965	1107	1062	2120	2100	880	860
Mongol Okhotsk	2869	2869	2191	2146	2900	2900	2240	2200
Mongolia	2011	1965	1107	1062	1940	1920	920	900
Sakhalin	1197	1152	474	429	880	860	440	420

3.1. Subduction initiation/cessation age interpretation

In the following regions, we interpret the ages of subduction initiation/cessation, based on a variety of published geological and geophysical observations.

3.1.1. North America

The western North American margin has seen long-lived subduction of the Farallon oceanic plate since at least the mid Mesozoic resulting in a myriad of accreted volcanic arc terranes along the west coast (DeCelles et al., 2009; Nokleberg et al., 2000; Ward, 1995). A number of detailed seismic tomographic studies show the slab material beneath the continent (Grand, 1994; Liu et al., 2008; Sigloch, 2011; Sigloch et al., 2008). The margin has been subject to various periods of subduction and back arc spreading as well as periods of flat slab subduction leading to a complicated geometry of subducted slab material (Sigloch and Mihalynuk, 2013). Subduction has been occurring since the late Triassic/early Jurassic, with the continued accretion of the Talkeetna, Bonanza and Stikine-Quesnellia arcs and formation of their associated subduction zones (Nokleberg et al., 2000). We take the approach of placing the base of the Farallon slab at between 195 and 175 Myr old (Nokleberg et al., 2000). This differs slightly from Van der Meer et al. (2010) who place its age between 208 and 180 Ma.

The North American profile (Figs. 2 and 3) highlights west dipping subducted Farallon oceanic lithosphere and was used by Van der Meer et al. (2010) as a key slab in order to constrain absolute plate motion. The Farallon slab (anomaly 1 in Figs. 2 and 4) is visible in all tomography models and reproduced in all three geodynamic model runs. The Hybrid Paleomagnetic and Hybrid TPW Paleomagnetic models reproduce the present day mantle structure observed in seismic tomography models better at the first order than the Subduction Reference Frame model, especially around lower mantle depths (~2000–2500 km). The Subduction Reference Frame model produces subducted material too far (10–15°) west of that imaged by tomography, especially in the mid to lower mantle. Given model sinking rates (~15–20 mm/yr), this material represents subduction occurring at around 100–130 Ma, where the corrections applied for longitude were between 14–18°. This suggests that longitudinal corrections to the absolute rotations are most-likely too great for the time period that corresponds to these depths, the surface subduction location from the plate model is offset, or the geodynamic model sinking rate is too high.

3.1.2. East Asia

The East Asian margin represents the location of long-lived subduction from the Mesozoic to the present day. Van der Meer et al. (2010) interpret at least 3 major phases of subduction corresponding to seismically fast anomalies within the mantle, which

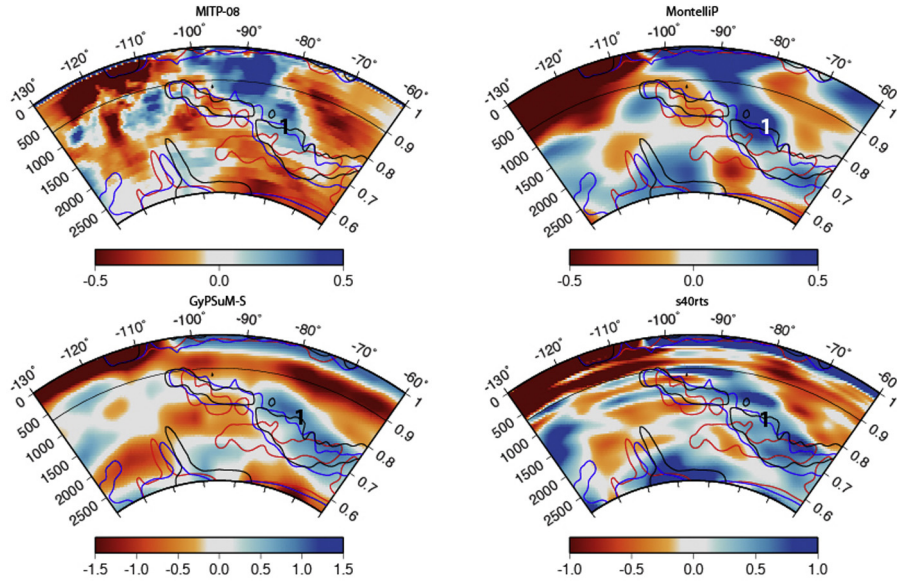


Fig. 2. Vertical cross section at 35° N. Anomaly 1 reflects subducted Farallon oceanic plate. Contours are the –200 K Terra temperature field output; blue contours represent the Hybrid Paleomagnetic model, black contours represent the Hybrid TPW Paleomagnetic model and red contours represent the subduction Reference Frame model. (For interpretation of the references to color in this figure legend, the reader is referred to the web version of the article.)

they term the Manchuria (upper, anomaly 1 in Fig. 4) Mongolian (mid-mantle, anomaly 2 in Fig. 4) and East China (lower mantle, anomaly 3 in Fig. 4) slabs. We interpret gaps in the tomography record as representing back arc spreading and the subduction of the IZanagi-Pacific ridge generating a visible slab window in the seismic tomography. Episodic magmatism within the Korean peninsula provides onshore geological constraints of this subduction, with three primary phases occurring (248–210 Ma, 197–158 Ma and 110–50 Ma) (Sagong et al., 2005). The 197–158 Ma phase and the 110–50 Ma phase are interpreted as being related to the East China and Mongolia slabs respectively, with the ~50 Myr gap from 158 Ma to 110 Ma representing back arc spreading and a shifting of volcanism offshore. Following subduction of the mid-mantle anomaly, interpreted as being IZanagi oceanic material, the Pacific–IZanagi ridge was subducted around 60–55 Ma (Whittaker et al., 2007), which led to a large scale plate reorganization and to a ~10 Myr

gap in the subduction record in the vicinity of subduction. The Manchuria slab is interpreted as Pacific lithosphere that has subducted since the IZanagi ridge subduction (50 Ma–present). The ages of slab material in East Asia cited (248–168 Ma for the East China Slab, 178–110 Ma for the Mongolia Slab and 80–present day for the Manchuria) by Van der Meer et al. (2010) were found to disagree with the ages cited by the record of episodic, subduction related magmatism in the Korean Peninsula (Sagong et al., 2005).

Latitudinal profiles through geodynamic model results and tomography models (Figs. 4 and 5) in East Asia show that the Subduction Reference Frame model produces the most inconsistent fit between model output and observed slab locations based on tomography out of the three scenarios tested, emplacing material too far (10–15°) to the west and in a much more discontinuous fashion, especially in the lower mantle (2000–2500 km). From the P-wave models, both the Hybrid Paleomagnetic and the Hybrid

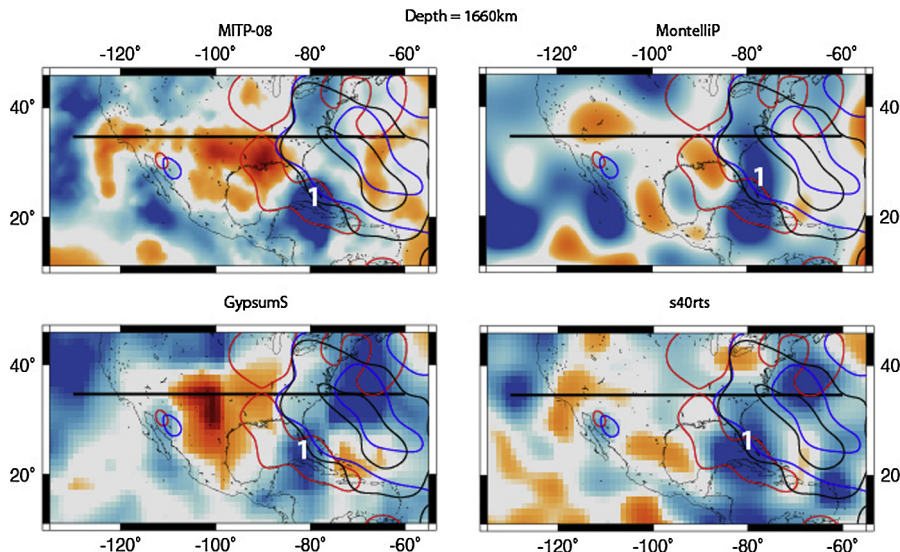


Fig. 3. Horizontal depth slices through tomography in the North American region at 1658 km depth. Contours same as Fig. 2. Anomaly 1 represents subducted Farallon oceanic lithosphere. The subduction reference frame model places material too far to the west compared to the other models and tomography.

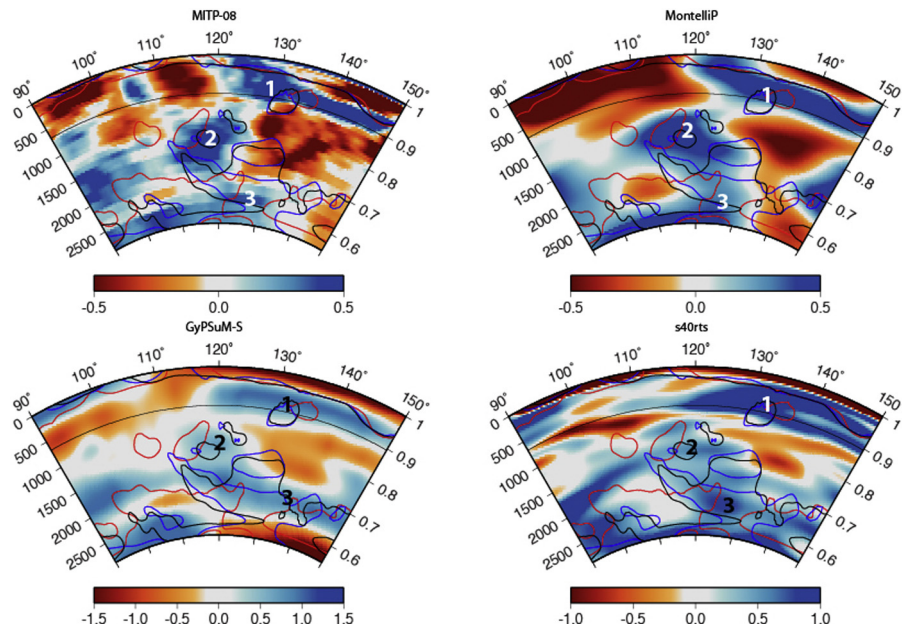


Fig. 4. Vertical cross sections at 48° N. Contours same as Fig. 2. Anomaly 1 represents Pacific material subducted after the Izanagi slab window formation (the Manchuria slab). Anomalies labeled 2 represent Izanagi material subducted prior to ridge subduction (the Mongolian slab). Anomalies labeled 3 represent older Izanagi material subducted between 197 and 158 Ma (the East China slab).

TPW Paleomagnetic model appear to emplace material slightly too far westward (~2–5°) at mid-mantle depths (1500–2000 km). However the S-wave models image fast anomalies here, indicating that relying on one tomography model can lead to erroneous conclusions.

3.1.3. Tethyan domain

The onset of subduction of the Neo-Tethyan Ocean slabs in the Mediterranean region is relatively well constrained. Initiation of subduction (i.e. the base of the Aegean Tethys slab) is dated using the obduction of the Vardar ophiolite complex in Greece at 168.5 ± 2.4 to 172.9 ± 3.1 Ma (Liati et al., 2004), the same geological

evidence used by Van der Meer et al. (2010). While the area is characterized by long-lived subduction, the regional mantle is quite heterogeneous, representing many different slab segments, with the slab associated with the Vardar ophiolites being spatially linked. As subduction is still currently ongoing in this area, dating the top of the slab is not required.

Van der Meer et al. (2010) identifies three independent slabs, the Himalayan, Maldives and Mesopotamia slabs, to represent subducted Neo-Tethyan lithosphere. The Himalayan slab is composed of material subducted between the docking of Burma (Heine et al., 2004) (~80 Ma) and the India Eurasia collision (~30 Ma). Our interpretation does not differ significantly from that of Van der

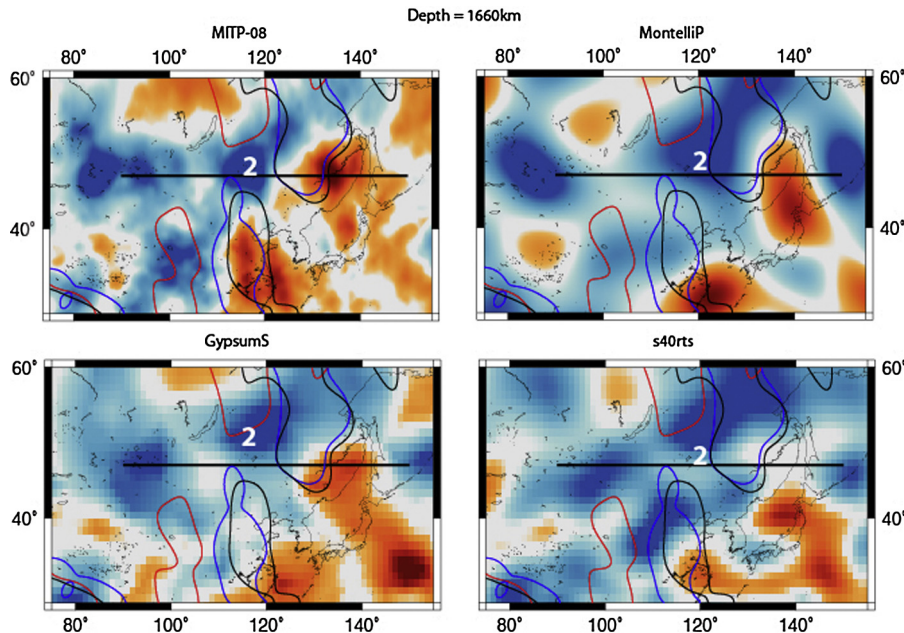


Fig. 5. Horizontal depth slices from tomography in the East Asian region at 1658 km depth. Contours same as Fig. 2. The Subduction Reference Frame model places material too far to the west compared to the other models and tomography.

Meer et al. (2010), who place inception at 85–79 Ma and cessation at 44–20 Ma. The Maldives slab formed from subduction of Meso-Tethyan lithosphere commencing with the docking of Tibet (~180 Ma) and ceasing with the docking of Burma and possible back arc spreading (Aitchison et al., 2007) prior to the India–Eurasia collision (~90–75 Ma). Previous interpretations place subduction inception at 220–200 Ma and cessation between 71 and 57 Ma (Van der Meer et al., 2010). The Mesopotamian slab formed from subducted Meso-Tethyan material that subducted to the northeast of the Maldives slab. We suggest that subduction began later here, with inferred subduction inception occurring ~165 Ma, based on the kinematic model by Müller et al. (2008), which differed from the Van der Meer et al. (2010) interpretation (subduction beginning between 220 and 200 Ma). The cessation of subduction is dated based on the obduction of the Semail ophiolite complex at approximately 79 Ma (Warren et al., 2003).

The central Indian Ocean profile (Figs. 6 and 7) images northward subducted Tethyan oceanic lithosphere, previously studied by Van der Voo et al. (1999a). The exact tectonic evolution of this area remains disputed (Aitchison et al., 2007; Lee and Lawver, 1995; Zahirovic et al., 2012), with alternate scenarios advocating fundamentally different pre-collision margin geometries. While this makes direct comparison of modeled slabs to tomography difficult, comparison of the distribution of material in the deep/mid mantle produced by different absolute rotations is possible. The Subduction Reference Frame model fits the tomography best, with the Hybrid Paleomagnetic model and Hybrid TPW Paleomagnetic model emplacing no material in the southern portion of the mid mantle (between 1000 and 2000 km and -10°S to 0°). When the horizontal extent of geodynamic model slab material at 2090 km is considered, it becomes apparent that the southern lower mantle material present in the Subduction Reference Frame model profile (anomaly 1, Fig. 7) originates from subduction along the western margin of the junction between the eastern Neo-Tethys and the Panthalassic Ocean (Seton and Müller, 2008). The geometry of this plate is poorly constrained as no geological evidence remains, so this match between slab positions resulting from the Subduction Reference Frame model with tomography provides valuable insights in determining paleo plate positions.

3.1.4. Central Asia

The deep mantle beneath central Asia is host to well constrained subducted material from the ancient Mongol-Okhotsk ocean basin that existed during the early-mid Mesozoic between the Siberia craton and the North and South China blocks. The slabs underneath central Asia have been studied previously (Van der Voo et al., 1999b). The timing of closure for the Mongol-Okhotsk ocean is constrained by the suture zone between Siberia and the North China block, placing the cessation of subduction at approximately 150 Ma (Kravchinsky et al., 2002; Van der Voo et al., 1999b), later than that inferred by Van der Meer et al. (2010) (180–155 Ma). However, onset of subduction of the Mongol-Okohtsk ocean remains elusive and, as slab material lies along the CMB, age estimates inferred from sinking rates are likely to be erroneous due to cessation of sinking and lateral spreading along this chemical boundary.

3.1.5. North Pacific

The Circum North Pacific is the location of complex long-lived subduction. Van der Meer et al. (2010) interpret 5 different slabs in this area: The Aleutian, Beaufort, Chuckchi, Kamchatka and Sakhalin slabs. The Aleutian slab is composed of Pacific material subducted northwards since approximately ~50 Ma (Gorbatov et al., 2000; Qi et al., 2007). This interpretation differs slightly from the 84 to 52 Ma subduction beginning inferred by Van der Meer et al. (2010). The Beaufort slab formed due to subduction along the northeastern Eurasian margin, between ~200 and ~155 Ma

(Nokleberg et al., 2000), roughly the same as inferred by Van der Meer et al. (2010). The Chuckchi slab formed from material subducted between the inception of the Koyukuk arc (~160 Ma Nokleberg et al., 2000) and the subduction of the Izanagi-Farallon ridge and subsequent transform margin formation at ~130 Ma. Previous interpretations of subduction cessation were between 120 and 100 Ma (Van der Meer et al., 2010). The Sakhalin and Kamchatka slabs are the result of spatially linked subduction events along the Asian-Arctic margin, with subduction beginning at ~65 Ma for the Sakhalin slab and ~60 Ma for the Kamchatka slab (inferred from the convergence history based on the topological plate polygons/rotations for this region (Clark and Müller, 2008; Gurnis et al., 2012). The Sakhalin slab terminated subduction shortly after this with the subduction of the northernmost portion of the Izanagi-Pacific ridge at ~50 Ma (Whittaker et al., 2007), while the Kamchatka subduction continues to the present day. This differs substantially from previous interpretations, which placed subduction initiation between 100 and 84 Ma for both slabs (Van der Meer et al., 2010).

Unintentionally, the reinterpreted slabs are mostly confined to the northern hemisphere and under continental crust. Most likely this is due to the better-resolved tomography in the northern hemisphere and the geological constraints available in these regions. There is no reason for a significant difference between north and south hemisphere sinking rates.

4. Discussion of geodynamic models

Agreement between geodynamic model output and seismic tomography in both the upper and lower mantle is only moderate-low (Figs. 2–7). This is most likely due to both the complexity of the tomography and the relative simplicity of the modeling code, where downwellings are modeled symmetrically. This is especially evident along the East Asia Subduction zone (Fig. 4). As we aim to assess the global models however, moderate-low agreement is sufficient. It is also evident along the Farallon Subduction zone, where none of the models emplace material where it is observed in the mid-mantle (Fig. 2). This could be due to the effects of flat slab subduction, which has not been included in the model. Another thing which contributes to the mismatch between the model output and tomography is errors in the input plate kinematic reference frame, suggesting that reference frame refinement is necessary. This is also possibly evident below East Asia (Figs. 4 and 5), where the modeled results don't reproduce the extent of the tomographically inferred slabs very well. However, because geodynamic model results do reproduce the location to some extent, this indicates that kinematic model refinement is required, especially in the pre-83.5 Ma Pacific basin.

The primary difference between geodynamic model output stems from the different input absolute reference frame paleo-longitude of subduction zone locations. This is apparent in the geodynamic model output, as the locations of subduction zones mark the areas of convergence and hence slab sinking. The heterogeneity in subduction zone paleo-longitudinal position at 140 Ma, the age at which our plate models begin, can be seen in Fig. 1.

The locations of subducted material in the upper mantle resulting from modeling all three absolute reference frames are very similar. Using an intersecting polygon analysis (Shephard et al., 2012, SOM) we quantify the relative location of geodynamic model slab material. We find overlap of slab material for the Hybrid Paleomagnetic and the Hybrid TPW geodynamic models with the Subduction Reference Frame model to be 77% and 75%, respectively. Similarities are expected because longitudinal differences between the alternate absolute reference frames in the Cenozoic are not large. During the Cenozoic, both the Hybrid Paleomagnetic and

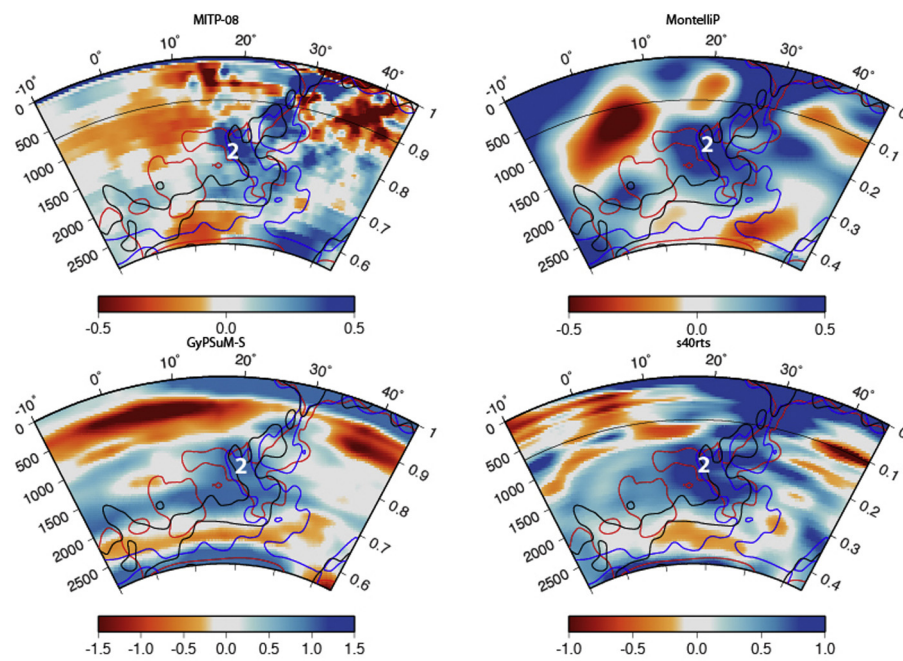


Fig. 6. Vertical cross sections at 80° E. Anomaly 2 represents material subducted prior to the closing of the Tethys Ocean. Contours same as Fig. 2.

Hybrid TPW Paleomagnetic model utilize moving hotspots, while the Subduction Reference Frame model uses the same rotations only slightly corrected to place surficial geological data above the anchor slabs. Further back in time (i.e. 80–140 Ma), in several areas with sufficiently well resolved plate kinematic constraints, such as East Asia and Western North America, the Subduction Reference Frame model fails to reproduce first order tomographic observations accurately (Figs. 2 and 4). The longitudinal corrections resulting from the Van der Meer et al. (2010) approach during the mid-late Cretaceous are likely too large, as such the Subduction Reference Frame model places anchor slab material between 8–12° too far westward compared to the equivalent slab positions from seismic tomography. The Hybrid Paleomagnetic and Hybrid TPW Paleomagnetic model result in an average of 6–9° westerly offsets from seismic tomography.

By considering subduction in a fully convecting mantle we build upon simple correlation of subduction/paleo subduction zones and tomographically interpreted slabs. Lateral slab motion induced by this flow would be greatest in the upper-mantle low-viscosity zone, and the lowermost mantle due to slab pile-up and spreading along the CMB. Similar studies on the effect of variable viscosity on 3 dimensional convection show that rms velocities (and thus lateral slab migration) are highest in the lowermost and uppermost mantle (Tackley, 1996).

Evidently, the plate reconstruction input into the geodynamic models dictates the evolution of the slabs. The apparent agreement between tomography and geodynamic modeling suggests that the comparison between the two can help us understand slab dynamics. However, the mismatch between the two in some locations implies that the initial reconstructions may require amendment.

5. Slab sinking

While deep mantle anomalies interpreted as subducted slabs do offer the best possible constraint on absolute plate motion, errors can easily arise if the wrong sinking velocities are used. This becomes readily apparent when maps of mantle tomography and plate reconstructions are superimposed. If regional sinking rates differ from global average rates, as is the case in many regions

(Fukao et al., 2009; Sigloch, 2011; Supplementary Information), no one depth slice accurately represents a particular geological time. The Subduction Reference Frame we tested relied on rotating surficial evidence of subduction over interpreted mantle velocity anomalies, relying on three primary anchor slabs, the Farallon, Aegean Tethys and Mongol-Okhotsk slabs (Van der Meer et al., 2010). Subduction history at each of these areas is complicated and associated with different sinking rates ranging from 8 to 15 mm/yr. As the Mongol-Okhotsk slab lies along the CMB, it is likely to have a slower than average sinking rate due to it being basally supported, and is likely to have spread laterally along the CMB. Previous studies also indicate that sinking rates in this area are lower than average (~10 mm/yr) (Van der Voo et al., 1999b). The Aegean Tethys slabs location and age of subduction initiation indicates a sinking rate of ~12 mm/yr, while the Farallon slabs depth and age implies a sinking rate of ~14 mm/yr (Tables 2–4). While these sinking rates are based on a simple age-depth correlation, they illustrate the possible differences in age of any single depth slice.

Inferences about slab sinking are apparent when considering tomography and our modeling results. Owing to the large viscosity contrast between the upper and lower mantle, at least two different depth-dependent sinking rates are evident (Conrad and Lithgow-Bertelloni, 2002; Goes et al., 2008; Hafkenscheid et al., 2006; Jarvis and Lowman, 2007; Marton et al., 1999; Morra et al., 2010; Stegman et al., 2010a,b,a,b). Under ideal conditions, initial slab sinking velocity is determined by negative buoyancy and viscosity of the surrounding mantle. Therefore the velocity at which a plate advances at the surface is close to the density-driven sinking velocity (Goes et al., 2008; Hafkenscheid et al., 2006; Lithgow-Bertelloni and Richards, 1998; Ricard et al., 1993; Schellart, 2004). However, observations from seismic tomography indicate that slabs sinking vertically and penetrating into the lower mantle through the transition zone without delay is commonly not the case, with both partial penetration and build up of material (slab stagnation) being observed (Fukao et al., 2009; Sigloch, 2011; Stegman et al., 2010a,b). Modeling suggests that trench migration is a key factor influencing slab penetration into the lower mantle (Christensen, 1996; Griffiths et al., 1995; Guillou-Frottier et al., 1995) and that material can stagnate along this boundary for tens of millions of years until

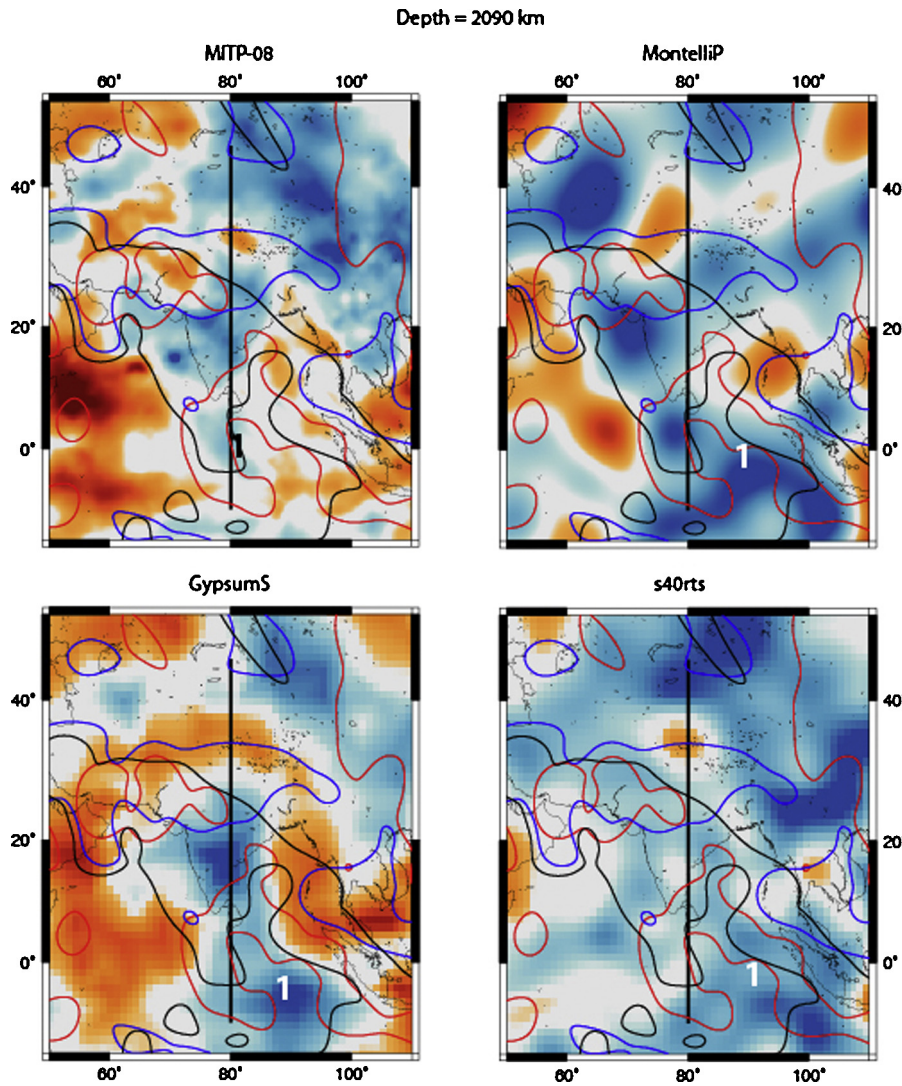


Fig. 7. Horizontal slices from tomography of the Indian region at 2093 km depth. Anomaly 1, representing material subducted beneath the east dipping Junction Subduction zone, is far more offset to the east in the Subduction Reference Frame model. Anomaly 2 is placed at a similar position in all three models. Contours same as Fig. 2.

enough material builds up and a ‘mantle avalanche’ occurs (Tackley et al., 1993; Pysklywec and Mitrovica, 1998). Differential sinking in adjacent areas has been noted in the North American mantle, with interpreted younger slab segments being observed deeper than older fragments due to the bistable nature of the transition zone (Sigloch, 2011). Numerous mechanisms have been proposed to cause heterogeneity of slab morphology in the upper mantle, from the Stokes buoyancy and flexural stiffness of the subducting plate (Stegman et al., 2010a,b,a,b,a,b), trailing edge boundary conditions and slab width (Stegman et al., 2010a,b,a,b), slab dip angle, possible lateral differences in rheological strength (Sigloch, 2011) and plume–slab interaction (Obrebski et al., 2010).

Sinking velocities in the mantle are strongly influenced by a viscosity jump of between 1 and 3 orders of magnitude between the upper and lower mantle (Goes et al., 2008; Hafkenscheid et al., 2006; Jarvis and Lowman, 2007; Marton et al., 1999; Morra et al., 2010; Ricard et al., 1993; Stegman et al., 2010a,b,a,b,a,b; Van der Meer et al., 2010). Numerous techniques have been used to approximate the effect of this viscosity jump on plate sinking velocity. Lithgow-Bertelloni and Richards (1998) use a relationship between upper and lower mantle sinking velocity, where lower mantle sinking velocities were obtained from the formula $v_T = (1/s)v_C$, where v_T is the slab’s terminal velocity, s is the slowing factor, and v_C is

the plate convergence rate. The slowing factor, s , is taken as proportional to the natural logarithm of the viscosity contrast between the upper/lower mantle based on theoretical convection studies with depth dependent viscosity (Gurnis and Davies, 1986; Richards et al., 1991; Ricard et al., 1993). This commonly leads to lower mantle slab sinking rates on the order of 10–30 mm/yr, which agrees with other approaches (Goes et al., 2008; Hafkenscheid et al., 2006; Lithgow-Bertelloni and Richards, 1998; Ricard et al., 1993; Stegman et al., 2010a,b,a,b,a,b). Higher rates of slab sinking are associated with areas of abundant subduction (Stegman et al., 2010a,b,a,b,a,b). Steinberger (2000) uses seismic heterogeneity in the lowermost mantle in concordance with Mesozoic and Cenozoic Subduction history to conclude that it takes on the order of 120 Myr for slabs to reach the core–mantle boundary (CMB), suggesting lower mantle sinking rates of around 17 mm/yr. A reduction of sinking speed by a factor of 4 upon entering the lower mantle is used by Schellart et al. (2009) to compute sinking rates in accordance with Lithgow-Bertelloni and Richards (1998) and a rate of 15 mm/yr was obtained. As a separate test, the velocity of a sinking oblate ellipsoid, $v_E = ((SD^2 g(\rho_S - \rho_M))/(18\mu_{LM}))$ (Kerr and Lister, 1991), can be used to evaluate mantle sinking rates (where v_E is the velocity of an oblate spheroid, $D = (abc)^{1/3}$ where a , b , and c are the ellipsoid axes, S is a shape factor relating to the physical dimensions of the ellipsoid also

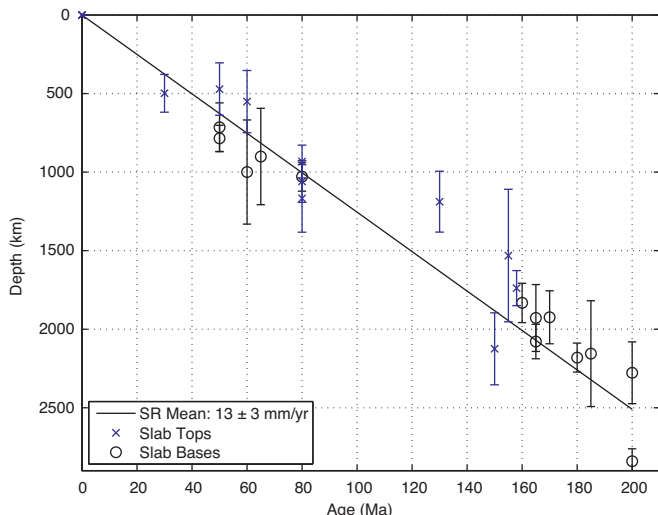


Fig. 8. Age-depth plot of reinterpreted slab depths and ages (Tables 2–4) in the lower mantle. The line of best fit reflects an average fit to all model interpretations, leading to an average sinking rate of 13 ± 3 mm/yr, slightly faster than the rate of 12 mm/yr proposed by Van der Meer et al. (2010). Depth errors are standard deviations of all the tomography models' slab depths (Supplementary Information). Age errors are poorly constrained by the literature, and thus are not considered.

depending on a , b , and c , $\rho_S - \rho_M$ is the density contrast between slab and mantle, and μ_{LM} is the viscosity of the lower mantle). Schellart et al. (2009) applied this relationship to the South Loyalty slab, yielding a sinking velocity of 13 mm/yr, which is close to that based on the Lithgow-Bertelloni and Richards (1998) method.

5.1. Sinking rates from geological evidence

Numerous authors have attempted to estimate average sinking velocities using the spatial distributions of deep mantle slabs and their relation to surface geology features (Hafkenscheid et al., 2006; Van der Meer et al., 2010; Van der Voo et al., 1999a,b). Examination of the tomographically imaged and geologically constrained slabs (Tables 2–4) yields a global average sinking rate in the entire mantle of 13 ± 3 mm/yr (Fig. 8). The error presented is the standard deviation of individual slab sinking rates. Stratified sinking rates that depend on a sinking rate reduction of approximately 4 at the upper/lower mantle transition zone (e.g. 52 mm/yr in the upper mantle compared to 13 mm/yr in the lower mantle) (Lithgow-Bertelloni and Richards, 1998; Schellart et al., 2009) place material far deeper than what is observed, especially in the upper to upper-mid mantle. This implies that either sinking rates in the upper mantle do not approximate plate convergence rates as commonly proposed in the literature (Goes et al., 2008; Hafkenscheid et al., 2006; Lithgow-Bertelloni and Richards, 1998; Ricard et al., 1993; Schellart, 2004) or more likely that slab stagnation in the transition zone has a significant effect on slab transit (Marton et al., 1999). This slab stagnation is apparent from examining many mantle provinces, especially the western Pacific and under North America (Fukao et al., 2009; Sigloch, 2011). While material may be sinking at rates comparable to plate velocity at the surface, the stalling and bending observed in high resolution tomography suggests significant resistance in slab transit. This has implications for attempting to use lower mantle slabs to constrain absolute plate motion: only slabs with a well-constrained history of sinking should be utilized for applying longitudinal corrections.

Upper/lower mantle viscosity contrast and initial slab geometry have the largest effect on increasing slab survival time within the mantle (Jarvis and Lowman, 2007). It follows that if there is a significant viscosity contrast between the upper and lower

mantle then slabs at least as old as 140 Myr could be visible. Thermal equilibration of slabs with adjacent mantle must also be taken into consideration. Van der Meer et al. (2010) also consider tomographic visibility and based on their reconstructions of past subduction zones, come to the conclusion that there are no slabs in the mantle older than approximately 300 Ma. When attempting to infer sinking rates from geological information, it is important to take into account the time it takes for slabs to sink all the way to the core mantle boundary (CMB). If mantle overturn time is shorter than the equilibration time, slabs will spread laterally along the core mantle boundary. Ricard et al. (1993) assume that thermal diffusion will not alter the long wavelength scale of mantle rocks on their timescale of interest (100–200 Myr) as the thermal diffusive length scale for 100 Myr is only on the order of 100 km.

The apparent misfit of higher upper mantle sinking rates, especially in the upper to upper-mid mantle (i.e. in the Tethys and Circum North Pacific) could be a manifestation of a number of processes. Slab material stalling at the transition zone is not accounted for in sinking rate calculations and could lead to a significant delay in sinking, possibly masking the faster upper mantle sinking rate. For example, if material were to stall in the transition zone for 10 Myr, this would imply subducted material of a given age would be 130 km shallower as compared to material passing through the transition zone without retardation (assuming a lower mantle sinking rate of 13 mm/yr). If material were to stall for 20 Myr, a plausible estimate given prior modeling (Pysklywec and Mitrovica, 1998), this would place material 260 km higher in the mantle. Our geodynamic models place slab material on the order of 100–300 km deeper than corresponding slabs inferred from tomography, suggesting that these stalling times need to be taken into account.

A possible viscosity change in the lower mantle between 1200 and 1500 km has been proposed, caused by a chemical phase transition of ferropericlase (Forte and Mitrovica, 2001; Morra et al., 2010). If this exists, we would expect to see a bend in the age-depth plot at this depth. Our results indicate that if this boundary exists it is not offering significant resistance to sinking slabs. To increase the robustness of this observation, more slabs in this proposed transition zone area would need to be studied.

The apparent fit of a globally uniform mantle sinking rate of 12 mm/yr in both the upper and lower mantle as proposed by Van der Meer et al. (2010) is due to the selection of dates used for the base and tops of slabs. The age-depth curve of Van der Meer et al. (2010) assigns ages of greater than 240 Myr to eight slabs that lie along the CMB. As material along this boundary stops sinking and flows laterally once reached, assigning older dates of deep material will skew the average sinking rate. Fig. 8 shows an age-depth curve, with only reinterpreted slabs used (Tables 2–4). This interpretation shows that average mantle sinking rates inferred from geological data alone are slightly greater than Van der Meer et al. (2010). That being said, due to complex sinking histories of well-imaged slabs (i.e. the Farallon, East Asian etc) global averages are insufficient for constraining absolute plate motion. Rather regional sinking rates should be used.

Other studies support the view that sinking rates need to be assessed on a regional basis, showing that lower mantle sinking varies regionally between approximately 10–20 mm/yr (Schellart et al., 2009; Van der Voo et al., 1999a,b). Indeed Schellart and Spakman (2012) use tomography and reconstructions to infer that sinking rates can vary even along individual subduction zones with upper mantle rates varying between 30 and 70 mm/yr and lower mantle sinking rates varying between 8 and 18 mm/yr along the Solomon-Vitiaz-Tonga-Kermadac-Hikurangi subduction zone. 13 mm/yr is a good approximation for a whole mantle sinking rate, as 20 mm/yr implies a much quicker mantle turnover (on the order of 130 Myr, compared to approximately 200 Myr inferred by a slower sinking rate). Geodynamic modeling using a viscosity

contrast of two orders of magnitude between the upper and lower mantle implies that mantle turnover of 130 Myr is not realistic, as modeling results using 130 Ma of plate history suffer from artifacts in the lowermost mantle, and inferences from using a mantle sinking rate derived from geological data alone indicate that 20 mm/yr is too high, placing material significantly deeper than observed. While sinking is sub-vertical due to the global flow dynamics, it is largely representative of natural sinking behaviors. Following this, sinking velocities from the geodynamic model used in this study were found to be on average ~50 mm/yr in the upper mantle and between ~15–20 mm/yr in the lower mantle. These values imply that material aged 140 Myr will be found between ~2600 km – CMB, thus depth comparisons with models starting at 140 Ma and tomography is suitable. Lateral slab motion introduced by considering slab sinking in a fully convecting mantle is known to be negligible, especially in the mid mantle. In the upper mantle, due to a low viscosity asthenosphere, and in the lowermost mantle due to slab pileup and spreading along the CMB, some lateral motion is expected (Bunge et al., 1997).

While including variable effects such as phase transitions at 410 and 660 km will potentially lead to more slab stagnation, they are deliberately not included in this study as the appropriate Clayperon slopes for a global model are not trivial due to the multiphase nature of downwelling material (Marton et al., 1999). Both the geological evidence and the flow dynamics inherent in our geodynamic models are consistent with a lower mantle two orders of magnitude more viscous than the upper mantle, and that a factor of 30 increase in viscosity between the upper and lower mantles previously used is not enough (Becker and Boschi, 2002; Liu et al., 2008). This is also consistent with geoid modeling studies of mantle viscosity structures (Lee et al., 2010; Schaber et al., 2009), which also indicate that a two order of magnitude difference between upper and lower mantle and a lower mantle viscosity of 10^{23} Pa s is realistic.

6. Conclusions

Three plate kinematic models have been used as input for three alternative geodynamic mantle convection simulations. The resulting output has been compared with four present-day mantle tomography models with the intention of improving our understanding of slab sinking dynamics in the mantle. All three geodynamic models produce westerly offsets compared with seismic tomography, with offsets increasing with depth, with the Subduction Reference Frame model producing the greatest misfits in the lower mantle. However, disagreement of slab material location between tomography, geodynamic models, and kinematic models, may imply poor absolute and relative plate motion constraints, slabs not sinking vertical, and poor resolution tomography, or a combination of these. Model results indicate that while subduction zone location is important in determining modeled mantle structure, plate velocity and hence slab input rates into the mantle are critical. Deciphering the depth of any particular slab is not straightforward, as the evolution of the slab since subduction is complicated; thus regional variations in slab sinking rates must be taken into account to avoid spurious global age-depth relationships. We have evaluated subducted slab sinking rates by combining alternative plate kinematic models, geological observations, mantle tomography, and geodynamic models. Our results converge on a globally averaged mantle sinking rate of 13 ± 3 mm/yr. Sinking rates from geodynamic modeling of 15–20 mm/yr indicate that rates of this magnitude are reasonable. Both the results from the geological data and modeling indicate that a viscosity contrast of two orders of magnitude between the upper and lower mantle is reasonable.

Acknowledgments

AST, RDM, MS and GES were supported by Australian Research Council Grants FL0992245, DP0987713 and LP0989312. This research is supported by the Science and Industry Endowment Fund. BSAS was supported by a Marie Curie Intra European Fellowship within the 7th European Community Framework Programme [FP7/2007–2013] under grant agreement no. 235861. CH is funded by ARC Linkage Project LP0989312 supported by Shell International E&P and TOTAL. We thank the DEISA Consortium (www.deisa.eu), co-funded through the EU FP6 project RI-031513 and the FP7 project RI-222919, for support within the DEISA Extreme Computing Initiative. We thank W.P. Schellart and an anonymous reviewer for their knowledgeable suggestions and insights for improving the manuscript; and N. Flament for fruitful discussions.

Appendix A. Supplementary data

Supplementary data associated with this article can be found, in the online version, at <http://dx.doi.org/10.1016/j.jog.2013.10.006>.

References

- Aitchison, J.C., Ali, J.R., Davis, A.M., 2007. When and where did India and Asia collide. *J. Geophys. Res.* 112, B05423.
- Amaru, M., 2007. Global travel time tomography with 3-D reference models. Utrecht University, pp. 1–174 (Ph.D. Thesis).
- Becker, T.W., Boschi, L., 2002. A comparison of tomographic and geodynamic mantle models. *Geochem. Geophys. Geosyst.* 3, 1003.
- Bunge, H.-P., 2005. Low plume excess temperature and high core heat flux inferred from non-adiabatic geotherms in internally heated mantle circulation models. *Phys. Earth Planet. Inter.* 153, 3–10.
- Bunge, H.-P., Baumgardner, J.R., 1995. Mantle convection modeling on parallel virtual machines. *Comput. Phys.* 9, 207–215.
- Bunge, H.-P., Richards, M.A., Baumgardner, J.R., 1996. Effect of depth-dependent viscosity on the planform of mantle convection. *Nature* 379, 436–438.
- Bunge, H.-P., Richards, M.A., Baumgardner, J.R., 1997. A sensitivity study of three-dimensional spherical mantle convection at 108 Rayleigh number: effects of depth-dependent viscosity, heating mode, and an endothermic phase change. *J. Geophys. Res.* 102, 11991–12007.
- Bunge, H.-P., Richards, M.A., Baumgardner, J.R., 2002. Mantle-circulation models with sequential data assimilation: inferring present-day mantle structure from plate-motion histories. *Philos. T. R. Soc. A* 360, 2545–2567.
- Christensen, U.R., 1996. The influence of trench migration on slab penetration into the lower mantle. *Earth Planet. Sci. Lett.* 140, 27–39.
- Clark, S.R., Müller, R.D., 2008. Convection models in the Kamchatka region using imposed plate motion and thermal histories. *J. Geodyn.* 46, 1–9.
- Conrad, C.P., Lithgow-Bertelloni, C., 2002. How mantle slabs drive plate tectonics. *Science* 298, 207–209.
- DeCelles, P.G., Dueca, M.N., Kapp, P., Zandt, G., 2009. Cyclicity in Cordilleran orogenic systems. *Nat. Geosci.* 2, 251–257.
- Doubrovine, P.V., Steinberger, B., Torsvik, T.H., 2012. Absolute plate motions in a reference frame defined by moving hot spots in the Pacific, Atlantic, and Indian Oceans. *J. Geophys. Res.* 117, B09101.
- Forte, A.M., Mitrovica, J.X., 2001. Deep-mantle high-viscosity low and thermochemical structure inferred from seismic and geodynamic data. *Nature* 410, 1049–1056.
- Fukao, Y., Obayashi, M., Nakakuki, T., 2009. Stagnant slab: a review. *Annu. Rev. Earth Planet. Sci.* 37, 19–46.
- Goes, S., Capitanio, F.A., Morra, G., 2008. Evidence of lower-mantle slab penetration phases in plate motions. *Nature* 451, 981–984.
- Gorbatschev, A., Widjiantoro, S., Fukao, Y., Gordeev, E., 2000. Signature of remnant slabs in the North Pacific from P wave tomography. *Geophys. J. Int.* 142, 27–36.
- Grand, S.P., 1994. Mantle shear structure beneath the Americas and surrounding oceans. *J. Geophys. Res.* 99, 11591–11621.
- Griffiths, R.W., Hackney, R.I., van der Hilst, R.D., 1995. A laboratory investigation of effects of trench migration on the descent of subducted slabs. *Earth Planet. Sci. Lett.* 133, 1–17.
- Guillou-Frottier, L., Buttles, J., Olson, P., 1995. Laboratory experiments on the structure of subducted lithosphere. *Earth Planet. Sci. Lett.* 133, 19–34.
- Gurnis, M., Davies, G.F., 1986. The effect of depth dependent viscosity on convective mixing in the mantle and the possible survival of primitive mantle. *Geophys. Res. Lett.* 13, 541–544.
- Gurnis, M., Turner, M., Zahirovic, S., DiCaprio, L., Spasojevic, S., Müller, R., Boyden, J., Seton, M., Manea, V., Bower, D., 2012. Plate Tectonic Reconstructions with Continuously Closing Plates. *Comput. Geosci.* 38, 35–42.

- Hafkenscheid, E., Wortel, M.J.R., Spakman, W., 2006. Subduction history of the Tethyan region derived from seismic tomography and tectonic reconstructions. *J. Geophys. Res.* 111, B08401.
- Hager, B.H., Richards, M.A., 1989. Long-wavelength variations in Earth's geoid: physical models and dynamical implications. *Philos. T. R. Soc. Lond. A* 328, 309–327.
- Heine, C., Müller, R.D., Gaina, C., 2004. Reconstructing the lost eastern Tethys ocean basin: convergence history of the SE Asian margin and marine gateways. *Geoph. Monogr. Ser.* 149, 37–54.
- Jarvis, G.T., Lowman, J.P., 2007. Survival times of subducted slab remnants in numerical models of mantle flow. *Earth Planet. Sci. Lett.* 260, 23–36.
- Kennett, B.L.N., Engdahl, E.R., Buland, R., 1995. Constraints on seismic velocities in the Earth from traveltimes. *Geophys. J. Int.* 122, 108–124.
- Kerr, R.C., Lister, J.R., 1991. The effects of shape on crystal settling and on the rheology of magmas. *J. Geol.* 99, 457–467.
- Kravchinsky, V.A., Cogné, J.P., Harbert, W.P., Kuzmin, M.I., 2002. Evolution of the Mongol-Okhotsk Ocean as constrained by new palaeomagnetic data from the Mongol-Okhotsk suture zone, Siberia. *Geophys. J. Int.* 148, 34–57.
- Lee, C.K., Han, S.C., Steinberger, B., 2010. Influence of variable uncertainties in seismic tomography models on constraining mantle viscosity from geoid observations. *Phys. Earth. Planet. In.* 184, 51–62.
- Lee, T.Y., Lawver, L.A., 1995. Cenozoic plate reconstruction of Southeast Asia. *Tectonophysics* 251, 85–138.
- Lévêque, J.J., Rivera, L., Wittlinger, G., 1993. On the use of the checker-board test to assess the resolution of tomographic inversions. *Geophys. J. Int.* 115, 313–318.
- Li, C., van der Hilst, R.D., Engdahl, E.R., Burdick, S., 2008. A new global model for P wave speed variations in Earth's mantle. *Geochem. Geophys. Geosyst.* 9, 1–21.
- Liati, A., Gebauer, D., Fanning, C.M., 2004. The age of ophiolitic rocks of the Hellenides (Vourinos, Pindos, Crete): first U-Pb ion microprobe (SHRIMP) zircon ages. *Chem. Geol.* 207, 171–188.
- Lithgow-Bertelloni, C., Richards, M.A., 1998. The dynamics of Cenozoic and Mesozoic plate motions. *Rev. Geophys.* 36, 27–78.
- Liu, L., Spasojevic, S., Gurnis, M., 2008. Reconstructing Farallon plate subduction beneath North America back to the Late Cretaceous. *Science* 322, 934–938.
- Marton, F.C., Bina, C.R., Stein, S., Rubie, D., 1999. Effects of slab mineralogy on subduction rates. *Geophys. Res. Lett.* 26, 119–122.
- Montelli, R., Nolet, G., Masters, G., Dahlen, F.A., Hung, S.H., 2004. Global P and PP traveltome tomography: rays versus waves. *Geophys. J. Int.* 158, 637–654.
- Morgan, J.W., 1983. Hotspot tracks and the early rifting of the Atlantic. *Tectonophysics* 94, 123–139.
- Morra, G., Yuen, D.A., Boschi, L., Chatelain, P., Koumoutsakos, P., Tackley, P.J., 2010. The fate of the slabs interacting with a density/viscosity hill in the mid-mantle. *Phys. Earth. Planet. Inter.* 180, 271–282.
- Müller, R.D., Sdrolias, M., Gaina, C., Roest, W., 2008. Age, spreading rates, and spreading asymmetry of the world's ocean crust. *Geochem. Geophys. Geosyst.* 9, Q04006.
- Nokleberg, W.J., Parfenov, L.M., Monger, J.W.H., Norton, I.O., Khanchuk, A.I., Stone, D.B., Scotes, C.R., Scholl, D.W., Fujita, K., 2000. Phanerozoic tectonic evolution of the Circum-North Pacific. USGS Professional Paper 1626.
- O'Neill, C., Müller, R.D., Steinberger, B., 2005. On the uncertainties in hot spot reconstructions and the significance of moving hot spot reference frames. *Geochem. Geophys. Geosyst.* 6, Q04003.
- Obrebski, M., Allen, R.M., Xue, M., Hung, S.H., 2010. Slab-plume interaction beneath the Pacific Northwest. *Geophys. Res. Lett.* 37, 1987–2004.
- Oeser, J., Bunge, H.-P., Mohr, M., 2006. Cluster design in the Earth Sciences Tethys. In: Gerndt, M., Kranzlmüller, D. (Eds.), High Performance Computing and Communications 4208. Springer, Berlin Heidelberg, pp. 31–40.
- Paulson, A., Zhong, S., Wahr, J., 2007. Inference of mantle viscosity from GRACE and relative sea level data. *Geophys. J. Int.* 171, 497–508.
- Pysklywec, R.N., Mitrovica, J.X., 1998. Mantle flow mechanisms for the large-scale subsidence of continental interiors. *Geology* 26, 687–690.
- Qi, C., Zhao, D., Chen, Y., 2007. Search for deep slab segments under Alaska. *Phys. Earth Plan. Inter.* 165, 68–82.
- Ricard, Y., Richards, M., Lithgow-Bertelloni, C., Le Stunff, Y., 1993. A geodynamic model of mantle density heterogeneity. *J. Geophys. Res.* 98, 21895–21909.
- Richards, M.A., Engebretson, D.C., 1992. Large-scale mantle convection and the history of subduction. *Nature* 355, 437–440.
- Richards, M.A., Jones, D.L., DePaolo, D.J., Duncan, R.A., 1991. A Mantle Plume Initiation Model for the Wrangellia Flood Basalt and Other Oceanic Plateaus. *Science* 254, 263–267.
- Ritsema, J., Deuss, A., van Heijst, H.J., Woodhouse, J.H., 2010. S40RTS: a degree 40 shear velocity model for the mantle from new Rayleigh wave dispersion, teleseismic traveltime and normal mode splitting function measurements. *Geophys. J. Int.* 184, 1223–1236.
- Sagong, H., Kwon, S.T., Ree, J.H., 2005. Mesozoic episodic magmatism in South Korea and its tectonic implication. *Tectonics* 24, TC5002.
- Schaber, K., Bunge, H.-P., Schuberth, B.S.A., Malervisi, R., Horbach, A., 2009. Stability of the rotation axis in high-resolution mantle circulation models: Weak polar wander despite strong core heating. *Geochem. Geophys. Geosyst.* 10, Q11W04.
- Schellart, W.P., 2004. Kinematics of subduction and subduction-induced flow in the upper mantle. *J. Geophys. Res.* 109, 1–19.
- Schellart, W.P., Kennett, B.L.N., Spakman, W., Amaru, M., 2009. Plate reconstructions and tomography reveal a fossil lower mantle slab below the Tasman Sea. *Earth. Planet. Sci. Lett.* 278, 143–151.
- Schellart, W.P., Spakman, W., 2012. Mantle constraints on the plate tectonic evolution of the Tonga-Kermadec-Hikurangi subduction zone and the South Fiji Basin. *Aust. J. Earth. Sci.* 59, 933–952.
- Schuberth, B.S.A., Bunge, H.-P., Ritsema, J., 2009a. Tomographic filtering of high-resolution mantle circulation models: Can seismic heterogeneity be explained by temperature alone? *Geochem. Geophys. Geosyst.* 10, Q05W03.
- Schuberth, B.S.A., Bunge, H.-P., Steinbe-Neumann, G., Moder, C., Oeser, J., 2009b. Thermal versus elastic heterogeneity in high-resolution mantle circulation models with pyrolite composition: High plume excess temperatures in the lowermost mantle. *Geochem. Geophys. Geosyst.* 10, Q01W01.
- Seton, M., Müller, R.D., 2008. Reconstructing the junction between Panthalassa and Tethys since the Early Cretaceous. *Eastern Australasian Basins III*, 263–266.
- Shephard, G.E., Bunge, H.-P., Schuberth, B.S.A., Müller, R., Talsma, A., Moder, C., Landgrebe, T.C.W., 2012. Testing absolute plate reference frames and the implications for the generation of geodynamic mantle heterogeneity structure. *Earth Planet. Sci. Lett.* 317, 204–217.
- Sigloch, K., 2011. Mantle provinces under North America from multifrequency P wave tomography. *Geochem. Geophys. Geosyst.* 12, Q02W08.
- Sigloch, K., McQuarrie, N., Nolet, G., 2008. Two-stage subduction history under North America inferred from multiple-frequency tomography. *Nat. Geosci.* 1, 458–462.
- Sigloch, K., Mihalynuk, M.G., 2013. Intra-oceanic subduction shaped the assembly of Cordilleran North America. *Nature* 496, 50–56.
- Simmons, N.A., Forte, A.M., Boschi, L., Grand, S.P., 2010. GyPSuM: A joint tomographic model of mantle density and seismic wave speeds. *J. Geophys. Res.* 115, 1–14.
- Stegman, D.R., Farrington, R., Capitanio, F., Schellart, W.P., 2010a. A regime diagram for subduction styles from 3-D numerical models of free subduction. *Tectonophysics* 483, 29–45.
- Stegman, D.R., Schellart, W.P., Freeman, J., 2010b. Competing influences of plate width and far-field boundary conditions on trench migration and morphology of subducted slabs in the upper mantle. *Tectonophysics* 483, 46–57.
- Steinberger, B., 2000b. Slabs in the lower mantle—results of dynamic modelling compared with tomographic images and the geoid. *Phys. Earth Plan. Inter.* 118, 241–258.
- Steinberger, B., O'Connell, R.J., 1997. Changes of the Earth's rotation axis owing to advection of mantle density heterogeneities. *Nature* 387, 169–173.
- Steinberger, B., Torsvik, T.H., 2008. Absolute plate motions and true polar wander in the absence of hotspot tracks. *Nature* 452, 620–623.
- Steinberger, B., Torsvik, T.H., 2010. Toward an explanation for the present and past locations of the poles. *Geochem. Geophys. Geosyst.* 11, Q06W06.
- Steinberger, B., Torsvik, T.H., Becker, T.W., 2012. Subduction to the lower mantle – a comparison between geodynamic and tomographic models. *Solid Earth* 3, 415–432.
- Styles, E., Davies, D.R., Goes, S., 2011. Mapping spherical seismic into physical structure: biases from 3-D phase transition and thermal boundary layer heterogeneity. *Geophys. J. Int.* 184, 1371–1378.
- Tackley, P.J., Stevenson, D.J., Glatzmaier, G.A., Schubert, G., 1993. Effects of an endothermic phase transition at 670 km depth in a spherical model of convection in the Earth's mantle. *Nature* 361, 699–704.
- Tackley, P.J., 1996. Effects of strongly variable viscosity on three-dimensional compressible convection in planetary mantles. *J. Geophys. Res.* 101, 3311–3332.
- Talagrand, O., 1997. Assimilation of observations: An introduction. *J. Meteorol. Soc. Jpn.* 75, 191–209.
- Tarduno, J.A., Duncan, R.A., Scholl, D.W., Cottrell, R.D., Steinberger, B., Thordarson, T., Kerr, B.C., Neal, C.R., Frey, F.A., Torii, M., 2003. The Emperor Seamounts: southward motion of the Hawaiian hotspot plume in Earth's mantle. *Science* 301, 1064–1069.
- Torsvik, T.H., Müller, R.D., Van der Voo, R., Steinberger, B., Gaina, C., 2008a. Global plate motion frames: toward a unified model. *Rev. Geophys.* 46, RG3004.
- Torsvik, T.H., Steinberger, B., Cocks, L.R.M., Burke, K., 2008b. Longitude: linking Earth's ancient surface to its deep interior. *Earth Planet. Sci. Lett.* 276, 273–282.
- Van der Meer, D.G., Spakman, W., van Hinsbergen, D.J.J., Amaru, M., Torsvik, T.H., 2010. Towards absolute plate motions constrained by lower-mantle slab remnants. *Nat. Geosci.* 3, 36–40.
- Van der Voo, R., Spakman, W., Bijwaard, H., 1999a. Mesozoic subducted slabs under Siberia. *Nature* 397, 246–249.
- Van der Voo, R., Spakman, W., Bijwaard, H., 1999b. Tethyan subducted slabs under India. *Earth Planet. Sci. Lett.* 171, 7–20.
- Ward, P.L., 1995. Subduction cycles under western North America during the Mesozoic and Cenozoic eras. In: Miller, D.M., Busby, C. (Eds.), *Jurassic Magmatism and Tectonics of the North American Cordillera*. *Geol. Soc. Am. Spec. Pap.* 299, , pp. 1–45.
- Warren, C.J., Parrish, R.R., Searle, M.P., Waters, D.J., 2003. Dating the subduction of the Arabian continental margin beneath the Semail ophiolite, Oman. *Geology* 31, 889–892.
- Wessel, P., Harada, Y., Kroenke, L.W., 2006. Toward a self-consistent, high-resolution absolute plate motion model for the Pacific. *Geochem. Geophys. Geosyst.* 7, Q03L12.
- Whittaker, J.M., Müller, R.D., Leitchenkov, G., Stagg, H., Sdrolias, M., Gaina, C., Goncharov, A., 2007. Major Australian-Antarctic plate reorganization at Hawaiian-Emperor bend time. *Science* 318, 83–86.
- Zahirovic, S., Müller, R.D., Seton, M., Flament, N., Gurnis, M., Whittaker, J., 2012. Insights on the kinematics of the India-Eurasia collision from global geodynamic models. *Geochem. Geophys. Geosyst.* 13, Q04W11.